Deformable Templates Using Large Deformation Kinematics

Gary E. Christensen, *Member, IEEE*, Richard D. Rabbitt, and Michael I. Miller, *Senior Member, IEEE*

***Abstract*— A general automatic approach is presented for accommodating local shape variation when mapping a two-dimensional (2-D) or three-dimensional (3-D) template image into alignment with a topologically similar target image. Local shape variability is accommodated by applying a vector-field transformation to the underlying material coordinate system of the template while constraining the transformation to be smooth (globally positive definite Jacobian). Smoothness is guaranteed without specifically penalizing large-magnitude deformations of small subvolumes by constraining the transformation on the basis of a Stokesian limit of the fluid-dynamical Navier–Stokes equations. This differs fundamentally from quadratic penalty methods, such as those based on linearized elasticity or thin-plate splines, in that stress restraining the motion relaxes over time allowing large-magnitude deformations. Kinematic nonlinearities are inherently necessary to maintain continuity of structures during large-magnitude deformations, and are included in all results. After initial global registration, final mappings are obtained by numerically solving a set of nonlinear partial differential equations associated with the constrained optimization problem. Automatic regridding is performed by propagating templates as the nonlinear transformations evaluated on a finite lattice become singular. Application of the method to intersubject registration of neuroanatomical structures illustrates the ability to account for local anatomical variability.**

I. Introduction

To meet the greater challenges of observing and tracking global biological shapes and structures, mathematical representations began to appear in the early 1980's under the name of *Grenander's global shape models*. Applications have appeared in human hands, cellular organelles, leaves, tracks, brains, and amoebas [1]–[10]. The global shape models represent image ensembles via the construction and deformation of typical image templates. Individual variabilities associated with the shapes of constituent biological structures are described using probabilistically constrained transformations applied to the templates. The transformations generate a rich family of shapes from a single template while maintaining its global properties. The ability to maintain, track, and recognize global structures in the presence of relatively large local image variability is one of the major advances of these approaches over conventional pixel-based imaging paradigms.

It is well known that biological structures, such as human neuroanatomies, vary in both global and local shape across a population. Although image volumes of two different normal brains may contain the same global structures—white matter, gray matter, ventricles, etc.—the internal structures will differ in shape, orientation, and fine structure. Our goal is to develop a method to represent the variabilities associated with individual neuroanatomies. The approach is to define the anatomical template as a three-dimensional (3-D) deformable continuum, with a deformation vector field applied throughout the continuum to provide a map from the individual anatomy back to the standard brain template. The vector field specifies the transformation.

We follow the approach defined in [6] and [11] to represent human neuroanatomies via deformable templates. The template is essentially an electronic atlas or anatomy atlas and individual variation is generated by deformation of the atlas coordinate system. The anatomical template is a vector function on the spatial *domain* $\Omega \subset \Re^3$ where Ω is often taken to be the unit cube. Throughout, each template within the atlas is assumed to be an N (typically 256) gray-level space corresponding to one or several imaging modalities. Variation is accommodated via the set of space-time transformations $\vec{h}(\cdot, \cdot) : \Omega \times [0, T] \rightarrow \Omega$. These transformations are generated from translations applied to the continuum evaluated on all points in Ω. The time-dependent displacement field $\vec{u}(\vec{x}, t)$ is defined in terms of $\vec{h}(\vec{x}, t)$ by the expression $\vec{h}(\vec{x}, t) = \vec{x} - \vec{u}(\vec{x}, t)$. The template is applied to individual subjects or anatomies by constructing the time-dependent (real or computational) map from the data volume $\{S(\vec{x}), \vec{x} \in \Omega\}$ back to points in the template to register the data with the atlas. The atlas and study (i.e., data) are said to be registered when the transformation is found that minimizes a consistent nonnegative distance measure $C(\cdot, \cdot)$ between the deformed atlas $T[\vec{x} - \vec{u}(\vec{x})]$ and the data $S(\vec{x})$, subject to constraints imposed by mechanics.

In order to represent complex anatomical patterns such as ventricles, cortical folds, etc., the transformations are represented by vector fields. Because these vector fields are infinite dimensional, regularization is required to ensure preservation of various topological properties of the mapping [12]. Such properties include preservation of landmarks or local maxima in the atlas images or connectedness of structures that would

Manuscript received October 25, 1994; revised November 12, 1995. This work was supported in part by the NSF under Presidential Young Investigator Award 8957206, the NIH under Grants R01-MH52158 and NIH-NCRR-RR01380, and by a grant from the Whitaker Foundation. The associate editor coordinating the review of this manuscript and approving it for publication was Prof. John J. Weng.

G. E. Christensen is with the Mallinckrodt Institute of Radiology, Washington University School of Medicine, St. Louis, MO 63110 USA (e-mail: gec@ee.wustl.edu).

R. D. Rabbitt is with the Department of Bioengineering, University of Utah, Salt Lake City, UT 84112 USA (e-mail: rabbitt@biomech.bioen.utah.edu).

M. I. Miller is with the Department of Electrical Engineering, Washington University, St. Louis, MO 63130 USA (e-mail: mim@ee.wustl.edu).

Publisher Item Identifier S 1057-7149(96)06029-0.

be associated with a positive Jacobian, and other smoothness features such as continuity of the mapping.

Our approach herein is to derive partial differential equations (PDE's) that the transformation fields must satisfy. The PDE's are crafted using principles obtained directly from continuum mechanics for deformable bodies. The deformation process does not attempt to model the physical process of brain growth; we use mechanical analogies to enforce topological properties that adhere to large deformation kinematics. Toward this end, the classical conservation equations of mechanics have been modified to account for nonmass-conserving deformations. This allows for the growth and shrinkage of regions within the continuum. When combined with the various constitutive laws (which have been well studied in continuum mechanics), we are provided with a mathematical framework that constrains our deformations with smoothness properties of which we have complete control. For example, under circumstances in which we do not choose to force the deformed template to stay close to its original configuration, the restricting force associated with large deformations can be relaxed while still maintaining smoothness of the deformation field. This PDE formulation is consistent with our previous work [2], [6], [11] based on Bayesian estimation by viewing the PDE as the minimizer of a posterior distribution (see the following section on choosing the body force).

A. Relationship to Previous Work

There has been a great deal of work done on multimodality image fusion, warping, and registration in a deformable anatomy context (see [13]–[15], for example). For much of the neuroanatomical work, the anatomical brain images being matched are assumed to be highly similar, requiring only global course features to be matched with rigid transformations (global rotation and translation) and/or simple scaling to match surface features and/or boundaries. For such cases, investigators often define a small number of features, surface or internal fiducials, and/or landmarks that serve to drive the registration, with high-dimensional transformations not required. The kinematics of the continuum and the associated PDE's that are proposed herein do not play a significant role for such transformations. Such low-dimensional rigid motions and or scale transformations are straightforwardly accommodated in our method as initial conditions.

Although the goal of image understanding is similar, the deformable template in this work differs fundamentally from deformable contour shape models such as those used in [16]–[18] and the deformable surface shape models such as those in [9] and [19]. In the previous approaches, deformable models correspond to parameterized contours and surfaces in a 2-D or 3-D image. These tend to be low-dimensional models, the dimension determined by number of control points on the curves or surfaces. The work proposed here requires volume transformations proportional to the number of pixels in 2-D or voxels in 3-D of the images being deformed.

The current work is perhaps most akin to the pioneering work in surface [20], [21] and solid deformation [22], [23], in which transformations are constructed to obey physical laws. The computerized surface models of facial motion apply local viscous damping. The deformable solid work for brain matching uses linear elastic penalties. For all such approaches, quadratic penalties derived for beams or solids are always used and the nonlinear kinematics of large deformations required to achieve a homeomorphism is ignored. Previous methods [2], [6], [24], [25] are limited in the sense already described. First, large magnitude displacements are severely penalized by regularization methods such as those based on linear elasticity or thin plates that develop restoring forces monotonically increasing with strain. Except for the smallest deformations, such penalties prevent full deformation of the template into the data. Secondly, these models are derived with small deformation approximations [26], [27] and are therefore not valid for large distance, nonlinear deformations. As we shall demonstrate, the transformations under these linear models do not enforce such physical properties such as 1-1 and smoothness of the transformation.

The contribution of this work is a new general approach for accommodating the large-distance, nonlinear kinematics required for transforming a template image into a target image when refining an initial global transformation. This is achieved by modeling the template as a highly viscous fluid allowing for large-magnitude, nonlinear deformations of small subvolumes. The resulting optimization problem is solved on an adaptive computational mesh associated with the propagated template. This work builds on and extends on previous work reported in [6], in which we describe an automatic, multiresolution approach for accommodating complex shape variation based on a linear elastic model. Some preliminary results of the current approach were provided in [8] for comparison to 3-D elastic deformations of neuroanatomical template images. The present work completes the presentation of the theory and provides details of the massively parallel computer implementation.

II. Dilatational-Viscous Fluid PDE

A. Eulerian Reference Frame and a Framework for Large Deformations

In describing large distance deformations, we use the Eulerian reference frame, as depicted in Fig. 1. The displacement field $\vec{u}(\vec{x}, t)$ is defined as a map from points in the template to fixed observation points in the deforming continuum, i.e., a mass particle instantaneously located at $\vec{x}$ at time t originated at point $\vec{x} - \vec{u}(\vec{x}, t)$. The Eulerian description of material deformations specifies the time evolution of particle positions and velocities as observed at fixed points. Because the data $S(\vec{x})$ is constant over the minimization procedure and the fact that it is stored as discrete voxels, $\vec{u}(\vec{x}, t)$ is parameterized by its spatial samples located at the center coordinate of each voxel of $S(\vec{x})$. Spatial tracking of the transformation in this manner allows very fine (on the order of voxel volumes) resolution structural variability to be accommodated.

In the Eulerian frame, accounting for the difference between the velocity $\vec{v}$ and the time rate of change of the deformation $\vec{u}$ is critical to using a fixed spatial grid to track the large deformation of templates. The material derivative, denoted

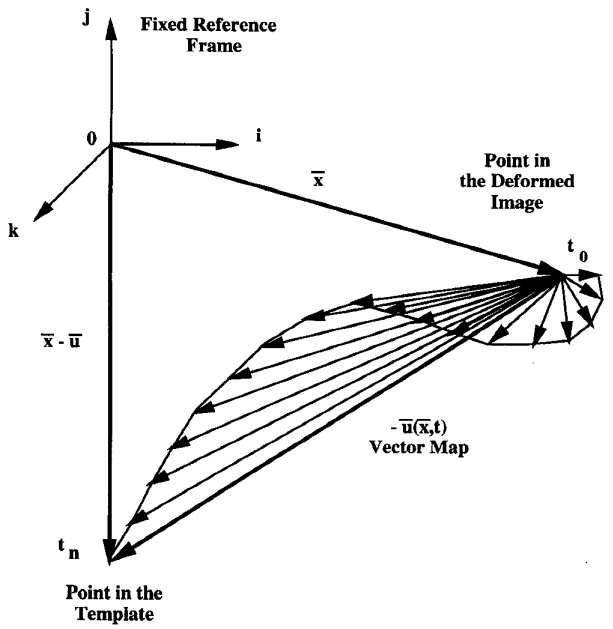

Fig. 1. Eulerian frame showing coordinate system used to track the kinematics of the deformation. In the Eulerian frame, vector and scalar field variables are associated with fixed spatial positions through which particles move rather than with moving material particles. The point $\vec{x}-\vec{u}(\vec{x}, t_i)$ denotes the particle from the template which is resident at location $\vec{x}$ at time t_i.

d/dt, provides the time rate of change experienced by an element of material instantaneously at point $\vec{x}$ at time t and is defined by $d/dt = \partial/\partial t + \sum_{i=1}^{3} v_i(\partial/\partial x_i)$ where $\vec{v} = [v_1(\vec{x}, t) \quad v_2(\vec{x}, t) \quad v_3(\vec{x}, t)]^T$. Using this, the velocity of an element of mass passing through $\vec{x}$ at time t is

$$\vec{v} = \frac{d\vec{u}}{dt} = \frac{\partial \vec{u}}{\partial t} + \sum_{i=1}^{3} v_i \frac{\partial \vec{u}}{\partial x_i} \tag{1}$$

where $\vec{u} = [u_1(\vec{x}, t) \quad u_2(\vec{x}, t) \quad u_3(\vec{x}, t)]^T$. The summation term in (1) accounts for the kinematic nonlinearities of the displacement field $\vec{u}$. Note that for small deformations the total material derivative with respect to time t and partial derivative with respect to time t are approximately equal.

B. Conservation of Momentum

We now derive the *conservation of momentum* equation, which gives the relationship between forces applied to the continuum and the resulting deformation. Consider a fixed control volume Ω with boundary $\partial\Omega$ and assume that a source supplies or extracts mass from the volume at a rate of η per unit volume. Distributed traction force $\vec{\tau}$ acts on the surface, and a distributed body force $\vec{b}$ per unit volume acts on all material elements within the body. Using i) Newton's second law in the form of conservation of linear momentum, ii) the fact that the traction force $\vec{\tau}$ is related to the Cauchy stress tensor $\mathbb{T}$ by $\vec{\tau} = \mathbb{T}\cdot\vec{n}$, where $\vec{n}$ is the outward unit normal from the surface, iii) the divergence theorem, and iv) the Reynolds transport theorem, modified to include a mass source (see Appendix A), gives the differential form of conservation of momentum

$$\rho \frac{d\vec{v}}{dt} + \vec{v}\eta - \vec{\nabla}\cdot\mathbb{T} - \vec{b} = \vec{0}. \tag{2}$$

where ρ is the density of the material. The notation $\vec{\nabla}\cdot\mathbb{T}$ is defined to be a 3×1 column vector with components $[\vec{\nabla}\cdot\mathbb{T}]_i = \sum_{j=1}^{3}(\partial T_{ij}/\partial x_j)$ where the components of $\mathbb{T}$ are $[\mathbb{T}]_{ij} = T_{ij}$ for i, j =1, 2, 3.

The momentum equation provides the relationship between applied body force $\vec{b}$, the state of stress, and the resulting material deformation. In the current approach, the body force $\vec{b}$ provides the connection between the sensor data and the deforming continua. The final form of the momentum equation (2) and associated generalized Lagrangian depends upon the constitutive behavior of the material, i.e., elastic, visco-elastic, Kelvin–Voight, etc.

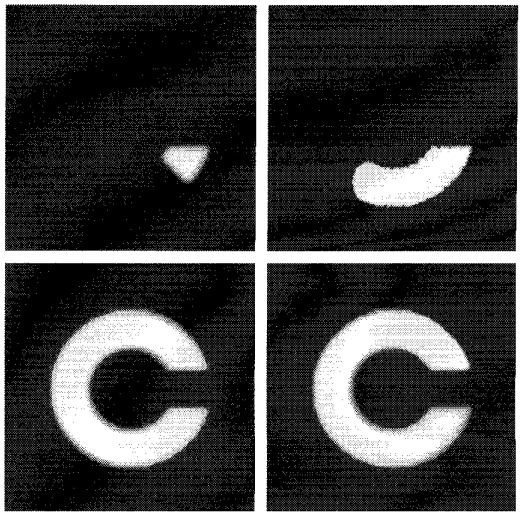

Fig. 2. The left column shows the template (top) and the study (bottom). The template was deformed into the study using an elastic-solid regularization (top right) and a viscous-fluid regularization (bottom right).

C. The Fluid Analog

We choose a constitutive law that allows for large, nonlinear deformations while maintaining a continuous homeomorphic map with smooth deformations of the template. This is an alternative constitutive law to Hooke's law used in linear elasticity, one corresponding to a viscous-fluid with the property that the stress within the deformed configuration is allowed to relax with time. This implies that the mechanical energy (penalty) does not (necessarily) increase with the magnitude of the pointwise deformation. A Navier–Poisson Newtonian fluid model is used, for which the Cauchy stress tensor $\mathbb{T}$ is related to the rate of deformation tensor D by $\mathbb{T} = [\lambda(\mathrm{tr}\, D) - p]\vec{I} + 2\mu D$, where μ and λ are the viscosity constants, p is the pressure, and the rate of deformation tensor is $D = 1/2[\vec{\nabla}\vec{v} + (\vec{\nabla}\vec{v})^T]$. Making these substitutions in (2) gives the modified Navier–Stokes equation $\mu\nabla^2\vec{v} + (\lambda + \mu)\vec{\nabla}(\vec{\nabla}\cdot\vec{v}) + \vec{b}(\vec{u}) = \vec{\nabla}p + \rho(d\vec{v}/dt) + \vec{v}\eta$. A simplified model is obtained for very low Reynold's number flow where the pressure gradient $\vec{\nabla}p$ and the inertial terms $\rho(d\vec{v}/dt) + \vec{v}\eta$ are

neglected, such that (2) becomes

$$\mu\nabla^2\vec{v} + (\lambda+\mu)\vec{\nabla}(\vec{\nabla}\cdot\vec{v}) + \vec{b}(\vec{u}) = \vec{0} \tag{3}$$

where $\nabla^2 = \nabla^T\nabla$ is the Laplacian operator. Without loss of generality, we assume that (3) is defined on $\Omega = [0, 1]^3 = \{\text{the unit cube}\}$ with the boundary conditions $\vec{v}(\vec{x}, t) = 0$ for $\vec{x} \in \partial\Omega$ and all t. The notation $\partial\Omega$ is defined as the boundary of Ω. Notice that when these boundary conditions are inserted into (1), the displacement on the boundary of Ω is zero, i.e., $\partial\Omega$ is mapped to $\partial\Omega$ under the fluid transformation.

The template is deformed by solving (3) subject to a body force $\vec{b}$ that drives the template viscously into registration with the study. Two mechanisms are clearly identified. The first, represented by $\mu\nabla^2\vec{v}$, is associated with constant volume viscous flow of the template. The second, represented by $(\lambda+\mu)\vec{\nabla}(\vec{\nabla}\cdot\vec{v})$, is nonzero when regions of the template grow or dissolve. Using continuity [(14), Appendix A] we note that $\vec{\nabla}\cdot\vec{v} = \eta/\rho - d\rho/dt$, so the second term in (3) is related to dilatation caused by the mass injection per unit volume η and the rate of change of density $d\rho/dt$. In the present work, we are specifically interested in allowing growth and shrinkage of local regions of the template and hence $\vec{\nabla}\cdot\vec{v}$ in general is nonzero. For the Navier–Poisson fluid employed here, the dilatational viscous stress resisting the rate of change of local volume is controlled by $[\lambda + (2/3)\mu]$, whereas the shear stress between adjacent regions is controlled only by μ.

D. The Body Force

A crucial part of the specification of the PDE in (2) is the force that drives the deformation of the template to match the configuration of the data. This force is induced by adopting the Bayesian view of the transformations, in which there exists a prior distribution on the transformations and the solution corresponds to a maximization of the posterior distribution relating the transformation fields to the data as collected by the sensor. The posterior is taken in Gibbs form with the total potential associated with the sum of the statistical model of the sensor and the prior distribution. The PDE formulation is then the variational maximizer (minimizer) of the Gibbs potential. The forcing function in the PDE is then none other than the variation of the sensor statistical likelihood function with respect to the vector displacement field [2], [6], [11].

This view is based on the existence of a variational principle from which the field equations can be induced; such principles are well known for conservative systems [28], [29] and link the PDE formulation as the minimizer (maximizer) of some potential (see Section V). Variational formulations have also been developed for numerous nonconservative systems, including a fluid model consistent with that addressed herein [30].

In this work, we use a Gaussian sensor model (likelihood)

$$C(T(\vec{x}), S\vec{u}(\vec{x},t)) = \frac{\alpha}{2}\int_\Omega |T(\vec{x} - \vec{u}(\vec{x},t)) - S(\vec{x})|^2\, d\vec{x} \tag{4}$$

where α is a constant. For magnetic resonance imaging (MRI) this appears to be reasonably appropriate [31]; for positron emission tomography (PET) and charge coupled device (CCD) data image reconstruction, Poisson models would be more appropriate [32], [33]. Others have investigated using the correlation [23]. Taking the variation of this cost function with respect to the displacement field yields the body force

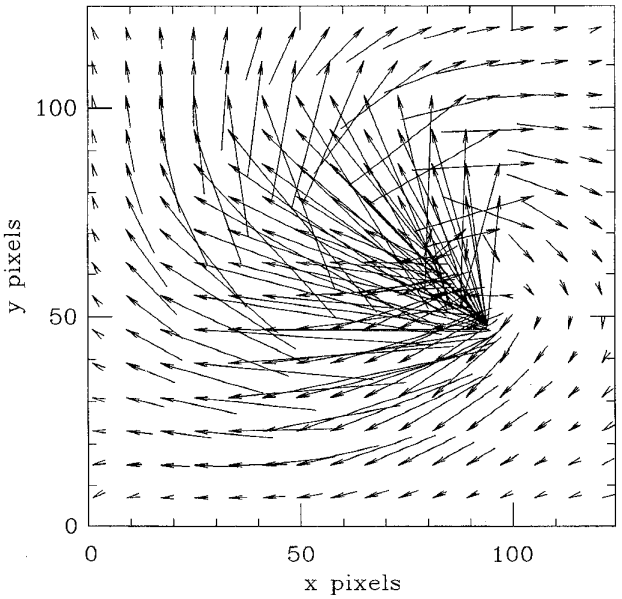

Fig. 3. Vector map of the viscous fluid transformation for the wedge-shaped patch to "C" experiment. The vectors shown here are only a subset of the full 128 × 128 vector field estimated in this experiment.

$$\vec{b}[\vec{x}, \vec{u}(\vec{x}, t)] = -\alpha(T[\vec{x} - \vec{u}(\vec{x}, t)] - S(\vec{x}))\vec{\nabla}T|_{\vec{x}-\vec{u}(\vec{x}, t)}. \tag{5}$$

The body force in (5) is composed of two terms. The term $\vec{\nabla}T|_{\vec{x}-\vec{u}(\vec{x}, t)}$, interpreted as $\vec{\nabla}_\xi T(\xi)$ evaluated at $\xi = \vec{x} - \vec{u}(\vec{x}, t)$, is the gradient of the template and has largest values at the edges of the structures in the template. This term determines the directions of the local deformation forces applied to the template. The second term $T(\vec{x}-\vec{u}(\vec{x}, t))-S(\vec{x})$ is the difference in intensity between the deformed template and the study. This term locally weights the first term. It is large when there is a large intensity mismatch and small otherwise. Notice that this second term causes the body force to be locally zero in areas where the deformed template is locally aligned with the study. The body force is globally zero when the deformed template and study are globally aligned.

The nonlinear deformation force given in (5) is evaluated directly and is not approximated. In contrast, others assume small deformations [23], [36] and linearize the body force using a Taylor series approximation. But since the motivation of the work presented herein is to allow large distance, nonlinear deformations, the small deformation assumption is not valid and linearization is not applicable.

Although the body force in (5) is a local operator, it generates the long distance forces required for deforming the template because the deforming continuum is coupled together by (3). The nonlinear dependence of the body force on $\vec{u}$ is required so that the body force remains consistent with the deformed template.

III. Numerical Solution

The solution of the viscous-fluid PDE given by (1), (3), and (5) includes nonlinearities associated with the body force and kinematic nonlinearities associated with the material derivative. In order to solve these nonlinear equations, the algorithm employs Euler integration in time combined with successive overrelaxation in the spatial domain. The nonlinear PDE is decomposed into a set of linear equations on the velocity field $v(x, t)$ for each instant of time t, and then integrated using the material derivative nonlinear relationship between the u and v fields.

Algorithm 1:

1) Initialize $t = 0$ and $\vec{u}(\vec{x}, 0) = 0$.
2) Using (5), calculate the body force $\vec{b}(\vec{x}, \vec{u}(\vec{x}, t))$ given $\vec{u}(\vec{x}, t)$.
3) If $\vec{b}(\vec{x}, \vec{u}(\vec{x}, t))$ is below a threshold for all $\vec{x} \in \Omega$ or the maximum number of iterations is reached, then STOP.
4) Solve the linear PDE (3) for the instantaneous velocity $\vec{v}(\vec{x}, t)$ at time t assuming that $\vec{v}(\vec{x}, t) = 0$, $\vec{x} \in \partial\Omega$. This is done using successive overrelaxation (SOR) [8].
5) Perform explicit Euler integration by calculating $\vec{u}(\vec{x}, t + \Delta)$ from the discretized version of the material derivative (1) given by $\vec{u}(\vec{x}, t + \Delta) = \vec{u}(\vec{x}, t) + \Delta\vec{v}(\vec{x}, t) - \Delta \sum_{i=1}^{3} v_i(\vec{x}, t)[\partial\vec{u}(\vec{x}, t)/\partial x_i]$.
6) Let $t = t + \Delta$ and go to Step 2.

Notice in Step 4 that the nonlinearity introduced by the body force term in (3) is handled by fixing $\vec{b}(\vec{x}, \vec{u}(\vec{x}, t))$ at time t. Since $\vec{b}(\vec{x}, \vec{u}(\vec{x}, t))$ is fixed for time t, solving for the instantaneous velocity is a linear problem. Also note in Step 4 that the assumption the velocity is zero on the boundary of Ω implies that the displacement field is also zero on the boundary of Ω. This assumption ensures that boundary of the deformed domain maps back onto the boundary of the original domain Ω through the identity mapping.

A. Solution on a Finite Spatial Grid

The viscous fluid PDE is solved on a discrete lattice associated with Ω. For large curved deformations, the transformation evaluated at these spatial grid points becomes singular over time even though the transformation evaluated on the continuum would not. To circumvent this problem, a method of regridding the template is used by generating a new, or propagated template, whenever the discretized transformation approaches local singularity. This is accomplished as follows.

The discretized displacement field is propagated through time using the procedure in the previous section until the Jacobian of the transformation indicates that the transformation is approaching singularity. When the magnitude of the Jacobian drops below a certain value, the computation is stopped and a new propagated template is generated equal to the deformed template at the previous instant. In the current implementation, a new template was propagated if the magnitude of the Jacobian dropped below a value of 0.5. A larger value causes more templates to be propagated, which will increase numerical precision errors of the transformation due to the increased number of concatenated transformations that need to be interpolated to obtain the total transformation. Conversely, a smaller propagation threshold causes less templates to be propagated. This may increase the numerical precision errors due to interpolating transformations that are nearly singular in places. The algorithm is restarted using the new template. When mapped back to the original template, this is equivalent to defining a new nonhomogeneous computation grid on the undeformed continua. Initial conditions for the propagated template are set to match the final state of the previous template, i.e., the instantaneous velocity remains the same and the displacement field corresponding to the new template is set to zero. The total transformation is continuously tracked via the concatenation of the displacement fields associated with all of the propagated templates.

We note that the above procedure assures that the concatenated transformation of the template into the study preserves the topology of the template. This is because each of the propagated template transformations preserve topology (due to the fact that the Jacobian of the transformation is positive globally) and the concatenation of topology-preserving transformations produces a topology-preserving transformation.

The method of propagating templates (i.e., regridding) is formalized in the following way. Let $T^{(j)}$, $j = 0, 1, 2 \cdots$ denote the sequence of propagated templates with associated displacement field $\vec{U}^{(j)}$, so that $T^{(j)}(\vec{x} - \vec{U}^{(j)}(\vec{x}, t_i))$ is the deformation of the jth template. Next, define t_{p_j} as the time that template $T^{(j-1)}$ is propagated to template $T^{(j)}$ such that $t_{p_0} = t_0 = 0 < t_{p_1} < \cdots < t_{p_M}$. Each propagated template $T^{(j)}$—except $T^{(0)}$, which is equal to the original template T—is defined as the deformation of the previous template $T^{(j-1)}$ at time t_{p_j}, as follows:

$$T^{(j)}(\vec{x}) \triangleq \begin{cases} T(\vec{x}), & j = 0, \\ T^{(j-1)}(\vec{x} - \vec{U}^{(j-1)}(\vec{x}, t_{p_j})), & 0 < j \leq M. \end{cases} \tag{6}$$

The time progression of displacement field $U^{(j)}$ becomes

$$\vec{U}^{(j)}(\vec{x}, t_i) \triangleq \begin{cases} 0, & i = p_j, \\ \vec{U}^{(j)}(\vec{x}, t_{i-1}) + (t_i - t_{i-1}) \\ \quad \cdot[\vec{v}(\vec{x}, t_{i-1}) - \Gamma_{i-1}\vec{U}^{(j)}(\vec{x}, t_{i-1})], & p_j < i \leq p_{j+1} \end{cases} \tag{7}$$

for $0 \leq i \leq N$ where p_0 and $\Gamma_i \triangleq \sum_{j=1}^{3} v_j(\vec{x}, t_i)(\partial/\partial x_j)$. This definition ensures that each propagated displacement field satisfies the discrete approximation of the material derivative (1) and that $T^{(j)}(\vec{x} - \vec{U}^{(j)}(\vec{x}, t_{p_j})) = T^{(j)}(\vec{x})$ at propagation time t_{p_j}. The displacement field $\vec{u}$ associated with the original template T is defined in terms of the propagated displacement fields $\vec{U}^{(j)}$ by

$$\vec{u}(\vec{x}, t_i) \triangleq \begin{cases} \vec{U}^{(0)}(\vec{x}, t_i), & 0 \leq i \leq p_1, \\ \vec{U}^{(j)}(\vec{x}, t_i) \\ \quad +\vec{U}^{(j-1)}(\vec{x} - \vec{U}^{(j)}(\vec{x}, t_i), t_{p_j}), & p_j < i \leq p_{j+1}. \end{cases} \tag{8}$$

Equation (8) is a consistency condition ensuring $T^{(0)}(\vec{x} - \vec{U}^{(0)}(\vec{x}, t_i)) = T(\vec{x} - \vec{U}^{(0)}(\vec{x}, t_i)) = T(\vec{x} - \vec{u}(\vec{x}, t_i))$, $0 \le i \le p_1$ and that $T^{(j)}(\vec{x} - \vec{U}^{(j)}(\vec{x}, t_i)) = T(\vec{x} - \vec{U}^{(j)}(\vec{x}, t_i) - \vec{U}^{(j-1)}(\vec{x} - \vec{U}^{(j)}(\vec{x}, t_i), t_{p_j})) = T(\vec{x} - \vec{u}(\vec{x}, t_i))$, $p_j < i \le p_{j+1}$. Incorporating (6)–(8) into Algorithm 1 gives the following algorithm.

Algorithm 2:

1) Let $t = 0$, $i = 0$, $T^{(0)}(\vec{x}) = T(\vec{x})$, and $\vec{U}^{(0)}(\vec{x}, 0) = 0$.
2) Calculate the body force $\vec{b}(\vec{x}, \vec{U}^{(i)}(\vec{x}, t)) = -(T^{(i)}[\vec{x} - \vec{U}^{(i)}(\vec{x}, t)] - S(\vec{x}))\vec{\nabla}T^{(i)}|_{\vec{x}-\vec{U}^{(i)}(\vec{x},t)}$.
3) If $\vec{b}(\vec{x}, \vec{U}^{(i)}(\vec{x}, t))$ is below a threshold for all $\vec{x} \in \Omega$ or the maximum number of iterations is reached, then STOP.
4) Solve the linear PDE (3) for the instantaneous velocity $\vec{v}(\vec{x}, t)$ at time t assuming that $\vec{v}(\vec{x}, t) = 0$, $\vec{x} \in \partial\Omega$ using SOR [8].
5) Calculate the perturbation of the displacement field $\vec{R}(\vec{x}) = \vec{v}(\vec{x}, t) - \sum_{i=1}^{3} v_i(\vec{x}, t)\,[\partial\vec{U}^{(i)}(\vec{x}, t)/\partial x_i]$.
6) Choose a real-time step size Δ which is a function of $\gamma = \max_{\vec{x}\in\Omega} ||\vec{R}(\vec{x})||$.
7) If the Jacobian of $\vec{x} - \vec{U}^{(i)}(\vec{x}, t) - \Delta\vec{R}(\vec{x})$ is less than 0.5, then propagate to template $i+1$ using $T^{(i+1)}(\vec{x}) = T^{(i)}(\vec{x} - \vec{U}^{(i)}(\vec{x}, t))$, $\vec{U}^{(i+1)}(\vec{x}, t) = 0$, set $i = i + 1$, and go to Step 5. Otherwise, update the ith displacement field using $\vec{U}^{(i)}(\vec{x}, t + \Delta) = \vec{U}^{(i)}(\vec{x}, t) + \Delta\vec{R}(\vec{x})$, set $t = t + \Delta$, and go to Step 2.

The next theorem states that under sufficiently smooth conditions on the transformation and velocity fields, the solution generated by Algorithm 2 solves the fluid PDE given by (1), (3), and (5) as $t_{i+1} - t_i$ goes to zero for all $0 \le i < N$. This, of course, proves that the regridding method allows large curved deformations to be calculated on a discrete grid while maintaining a diffeomorphism (i.e., avoiding a singular transformation).

Theorem 3.1: Let $\vec{U}^{(j)} \in C^2(\Omega)$ and $\vec{v} \in C^1(\Omega)$ where $\Omega \subset \Re^3$. Then Algorithm 2 satisfies the fluid PDE given by (1), (3), and (5) in the sense that for times t_i with $t_0 = 0 < t_1 < \cdots < t_N < T_{\max}$, the following system of equations are satisfied:

$$\mu\nabla^2\vec{v}(\vec{x}, t_i) + (\lambda + \mu)\vec{\nabla}[\vec{\nabla}\cdot\vec{v}(\vec{x}, t_i)] + \vec{b}(\vec{x}, \vec{u}(\vec{x}, t_i)) = 0 \quad (9)$$

$$\vec{u}(\vec{x}, t_i) = \begin{cases} 0, & i = 0 \\ \vec{u}(\vec{x}, t_{i-1}) + (t_i - t_{i-1}) \\ \quad \cdot[\vec{v}(\vec{x}, t_{i-1}) - \Gamma_{i-1}\vec{u}(\vec{x}, t_{i-1})] \\ \quad + o(t_i - t_{i-1}), & 0 < i \end{cases} \quad (10)$$

where $\Gamma_i \triangleq \sum_{j=1}^{3} v_j(\vec{x}, t_i)(\partial/\partial x_j)$ for $0 \le i \le N$.

Proof: Equation (9) is satisfied by Algorithm 2 if the real-time integration (10) is satisfied. Thus, it is only necessary to show that the real-time integration of Algorithm 2 given by (7) and (8) implies (10). We now show by induction that (7) and (8) satisfy (10).

Basis: Substituting (7) into (8) gives (10) for times $t_0 = t_{p_0} \le t_i \le t_{p_1}$.

Induction: Assume that Algorithm 2 satisfies (10) for time t_i and show that (10) is satisfied for t_{i+1}. Substituting (7) into (8) gives

$$\begin{aligned}\vec{u}(\vec{x}, t_{i+1}) = {} & \vec{U}^{(j)}(\vec{x}, t_i) + (t_{i+1} - t_i) \\ & \cdot[\vec{v}(\vec{x}, t_i) - \Gamma_i\vec{U}^{(j)}(\vec{x}, t_i)] \\ & + \vec{U}^{(j-1)}(\vec{x} - \vec{U}^{(j)}(\vec{x}, t_i) - (t_{i+1} - t_i) \\ & \cdot[\vec{v}(\vec{x}, t_i) - \Gamma_i\vec{U}^{(j)}(\vec{x}, t_i)], t_{p_j}).\end{aligned}$$

Using the fact that $\vec{U}^{(j-1)} \in C^2(\Omega)$, we can write the Taylor series expansion of $\vec{U}^{(j-1)}$ about the point $\vec{x} - \vec{U}^{(j)}(\vec{x}, t_i)$ as

$$\begin{aligned}\vec{u}(\vec{x}, t_{i+1}) = {} & \vec{U}^{(j)}(\vec{x}, t_i) + (t_{i+1} - t_i) \\ & \cdot[\vec{v}(\vec{x}, t_i) - \Gamma_i\vec{U}^{(j)}(\vec{x}, t_i)] \\ & + \vec{U}^{(j-1)}[\vec{x} - \vec{U}^{(j)}(\vec{x}, t_i), t_{p_j}] \\ & - (t_{i+1} - t_i)\vec{\nabla}\vec{U}^{(j-1)}|_{[\vec{x}-\vec{U}^{(j)}(\vec{x},t_i), t_{p_j}]} \\ & \cdot[I - \vec{\nabla}\vec{U}^{(j)}|_{(\vec{x},t_i)}]\vec{v}(\vec{x}, t_i) \\ & + o[(t_{i+1} - t_i)||\vec{v}(\vec{x}, t_i) - \Gamma_i\vec{U}^{(j)}(\vec{x}, t_i)||]\end{aligned}$$

where the (3×3) matrix $\vec{\nabla}\vec{u}$ is defined to have elements $[\vec{\nabla}\vec{u}]_{ij} = \partial u_i/\partial x_j$. Rearranging terms and using the fact that $\vec{v}$ and $\vec{\nabla}\vec{U}^{(j)}$ are bounded because they are continuous on the compact set Ω gives

$$\begin{aligned}\vec{u}(\vec{x}, t_{i+1}) = {} & (t_{i+1} - t_i)(\vec{v}(\vec{x}, t_i) - \Gamma_i(\vec{U}^{(j)}(\vec{x}, t_i) \\ & + \vec{U}^{(j-1)}(\vec{x} - \vec{U}^{(j)}(\vec{x}, t_i), t_{p_j}))) \\ & + \vec{U}^{(j)}(\vec{x}, t_i) + \vec{U}^{(j-1)}(\vec{x} - \vec{U}^{(j)}(\vec{x}, t_i), t_{p_j}) \\ & + o(t_{i+1} - t_i).\end{aligned}$$

Substituting (8) into this last expression gives (10) for time t_{i+1}. ■

IV. Results

Three experiments are presented in this section to demonstrate how the viscous fluid model accommodates large-distance, nonlinear deformations of small subregions of the template. The first two experiments are 2-D and the last 3-D. The fluid model was restricted from 3-D to 2-D by setting the velocity of the transformation in the third dimension to zero. In the resulting field, $\vec{\nabla}\cdot\vec{v} \neq 0$ such that $\eta/\rho + d\rho/dt \neq 0$. If we interpret individual elements of mass as maintaining constant density, then $d\rho/dt = 0$ and $\vec{\nabla}\cdot\vec{v} \neq 0$ implies action of a mass source such that $\eta \neq 0$. In this sense, the template "grows" into the configuration of the data.

We assume in all of the experiments that the template and the study agree topologically—i.e., both the template and study contain the same constituent structures with the same neighborhood structure—and that each constituent structure has roughly the same gray-level values. To guarantee a meaningful transformation, the template and the target must contain homologous topologies. It is important to note that 2-D data sets collected from 3-D volumes may not reflect the homology of the original 3-D space. To illustrate the influence of this, we have included results based on both 2-D and 3-D image data.

We also assume that the object of interest in the template and study object are padded in all directions by background.

The background in all of the experiments was assumed to be black (intensity zero). This requirement is due to the fact that the velocity of the displacement field along the boundary of the domain is zero in (3). Thus, the displacement along the boundary of the domain is zero.

Appropriate values of the viscosity coefficients λ and μ depend upon the particular imaging modality. Combining (3) and (5), we find the parameters λ/α and μ/α have units of "seconds" where we have assumed that the image data is normalized and nondimensional. For the present numerical results we take $\lambda/\alpha = 0.0$ and $\mu/\alpha = 0.01$ s. No attempt has been made to optimize these parameters or to study the influence of inhomogeneous properties on the results. These studies are left for future work.

A. The Patch to "C" Experiment

The first experiment shows how a small patch of material can deform into a longer curved patch of the same material. Fig. 2 shows a wedge-shaped template (top left) and a "C"-shaped study (bottom left) used in this experiment. The dimension of these images is 128×128 pixels. The template was initially aligned with the study so that they overlap. If this initial alignment was not performed, the algorithm would "stick" in a local minimum with the patch shrinking into a small point in order to minimize the cost (4).

Shown in the top right panel is the result of deforming the template into the study using the linear-elastic regularization (see Section V for details). Notice that the linear-elastic regularization method prevented the template from deforming into the study. The bottom right panel shows the result of the viscous-fluid regularization, which allows the template to more completely match the study. The difference in area of these objects is accommodated by the algorithm because conservation of mass is not enforced. The dilation of the material can be measured by evaluating the mass source term in (3).

A vector representation of the displacement field for the fluid transformation is shown in Fig. 3. Each displacement vector points from the original location of a material particle to its final location. Notice that the displacement vectors terminate on a regular grid but point to the very irregular set of corresponding locations in the textbook. This illustrates that the Eulerian framework for the displacement field provides the mapping from the study back to the original textbook.

The method of propagating templates used for solving the fluid PDE on a discrete grid is illustrated in Fig. 4 (cf., Section III). The top row shows propagated templates $T^{(4)}$, $T^{(12)}$, $T^{(18)}$, and $T^{(30)}$ (from left to right) that were used to deform the wedge-shaped patch into the "C." The second row of this figure illustrates the transformation applied to a rectangular grid for each propagated template. Notice that because the fluid transformation is continuous and globally one-to-one that the grid lines are continuous and do not cross over one another. The nonuniformity in the thickness of the deformed grid lines results from the fact that the original grid is expanded and compressed during the transformation. Notice the extent of the curved grid lines. This solution emphasizes the nature of the kinematics as manifest via the material derivative for accommodating nonlinear kinematic trajectories.

The third row of Fig. 4 shows the Jacobians of the transformations $\vec{x} - \vec{U}^{(i-1)}(\vec{x}, t_{p_i})$ that were used to determine the propagation times t_{p_i} for i = 4, 12, 18, and 30. Because the Jacobian of each propagated transformation $\vec{x} - \vec{U}^{(i-1)}(\vec{x}, t_{p_i})$ is greater than 0.5 for all $x \in \Omega$, the concatenation of the propagated transformations is continuous and globally one-to-one. The bottom row of Fig. 4 shows the Jacobian of the transformation $\vec{h}(\vec{x}, t_{p_i}) = \vec{x} - \vec{u}(\vec{x}, t_{p_i})$ evaluated at the propagation times i = 4, 12, 18, and 30. Notice that the Jacobian of $\vec{h}(\vec{x}, t_{p_i})$ is the Jacobian of the composition of the first $i - 1$ propagated transformations, corresponding to the product of the Jacobians of the first $i - 1$ propagated transformations.

B. 2-D Macaque Monkey Cryosection Data Experiment

The fluid transformation accommodates variation of structures with length scales on the order of the image resolution. This is precisely the kind of detail and accommodation of variability that we require for the cryosection brain data shown in Fig. 5. The top-left and top-middle panels of Fig. 5 show optical cryosection images of the visual cortex of two different macaque monkey brain slices. This cryosection data is at approximately $10\times$ the resolution of MRI data and it allows us to see the exquisite detail of the cortical mantle. This is illustrated via the dark gray folds interfacing to the white matter.

The result of using the fluid model to deform the template into the study is shown in the top-right panel. The template was first globally deformed into the study using the elasticity basis from [6]. Subsequent to the basis transformation, the fluid transformation was applied. Notice the similarity of the target (middle panel) and the transformed template (right panel). The left panel in the middle row shows the result of smoothly deforming a rectangular grid using this deformation. The x- and y-components of the displacement field are shown in the middle-middle and right-middle panels, respectively. Intensities that are close to white correspond to positive displacements; dark intensities correspond to negative displacements. The low spatial frequency intensity changes in displacements cause global shape changes and resulted from the elastic-solid transformation. The high spatial frequency intensity changes correspond to local shape changes resulting from the fluid transformation.

The fact that the transformation is smooth allows for the mapping of the anatomical information—known *a priori* for the template—to the target. The bottom row, left panel shows a gray/white matter segmentation of the template. The transformation of the template segmentation is shown in the bottom-right panel. This automatic segmentation of the study shows excellent agreement with a hand segmentation of the study shown in the bottom-middle panel. Discrepancies between the hand and automatic segmentation of the study are due, in part, to errors in the hand segmentation. Since the "accuracy" of the hand segmentation is not known, no attempt was made in this preliminary study to quantify differences between anatomic segmentations and hand segmentations.

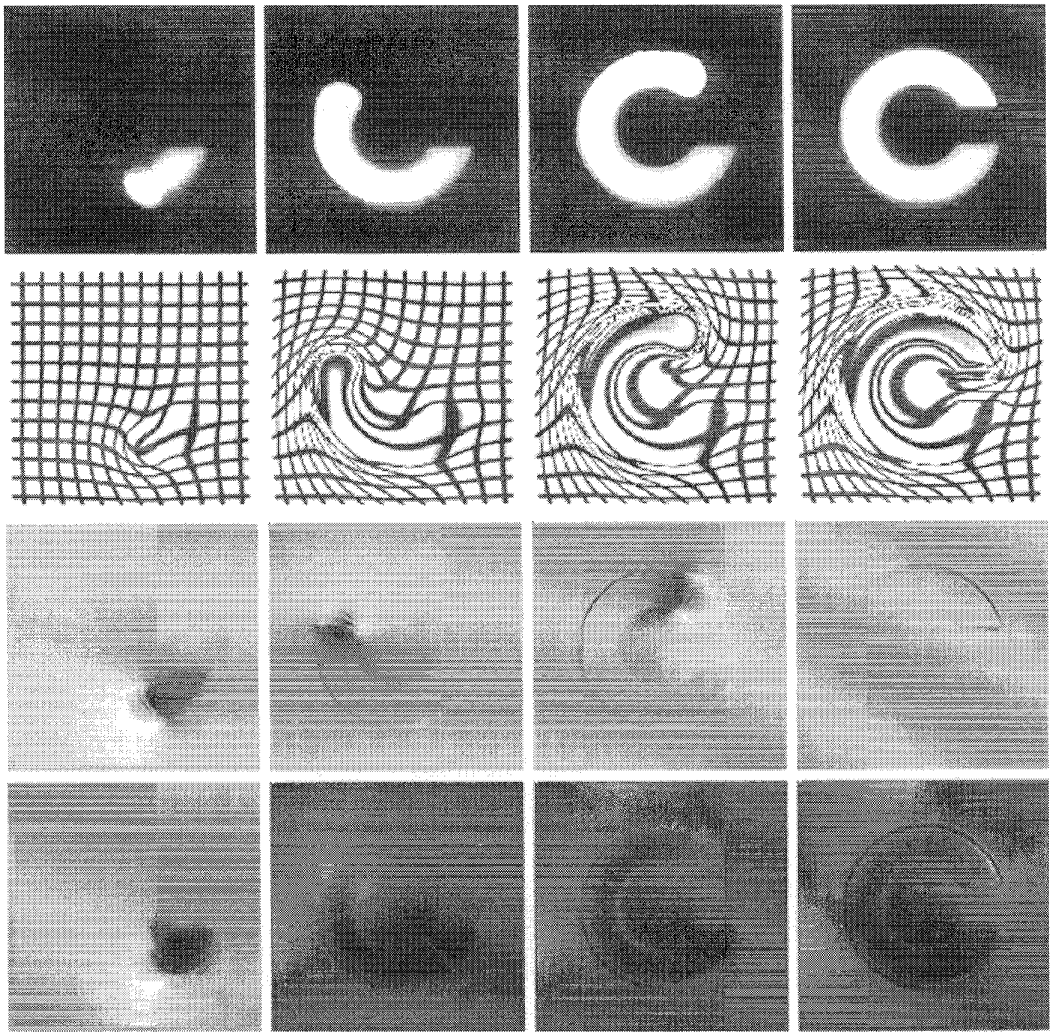

Fig. 4. The columns correspond to propagated templates: 4, 12, 18, and 30. The top row shows the propagated templates, the top middle row shows the time progression of the fluid transformation applied to a rectangular grid, the bottom middle row shows the Jacobians of the previous propagated transformations, and the bottom row shows the Jacobians of the transformations back to the original template.

C. 3-D Human MRI Experiment

As a final experiment, we demonstrate the fluid model applied to high-resolution 3-D MRI data of the human head. This experiment demonstrates that 3-D transformations are required to accommodate complex 3-D anatomical shape variation. The MRI data used was collected using an MPRAGE sequence. It was downsampled from 256 × 256 × 128 voxels at 1× 1× 1.25 mm^3 and symmetrically padded by zeros to produce 128 × 128 × 100 voxels at 2 mm^3. The range of intensities in the study image was preprocessed by histogram-matching it to the template.

The template was deformed into the shape of the study by first using the 3-D elastic basis method described in [8] to accommodate the global shape differences. This transformation was then refined using the 3-D fluid model to accommodate the local shape differences. The result of this experiment is shown in Fig. 6. The rows from top to bottom correspond to axial slices 48, 55, and 60, respectively, and the columns correspond to the template (left), the deformed template after the 3-D elastic basis method (middle left), the deformed template after the 3-D fluid method (middle right), and the study (right). Notice that, in both the global and local stages of the deformation, variation is accommodated in 3-D and is independent of the slice orientation. This is evident by the fact that structures appear and disappear from a fixed observation slice. The change of shape of the ventricles in the top row is a good illustration of this.

V. Discussion

A. Linear Elasticity

For purpose of comparison to previous work (see [2], [6], for example), it is interesting to examine Gaussian priors corresponding to such penalties as linearized elasticity. For a linear elastic solid the Cauchy stress tensor $\mathbb{T}$ relates to the strain tensor E by Hooke's law, $\mathbb{T} = \lambda_o(\mathrm{tr}\, E)I + 2\mu_o E$

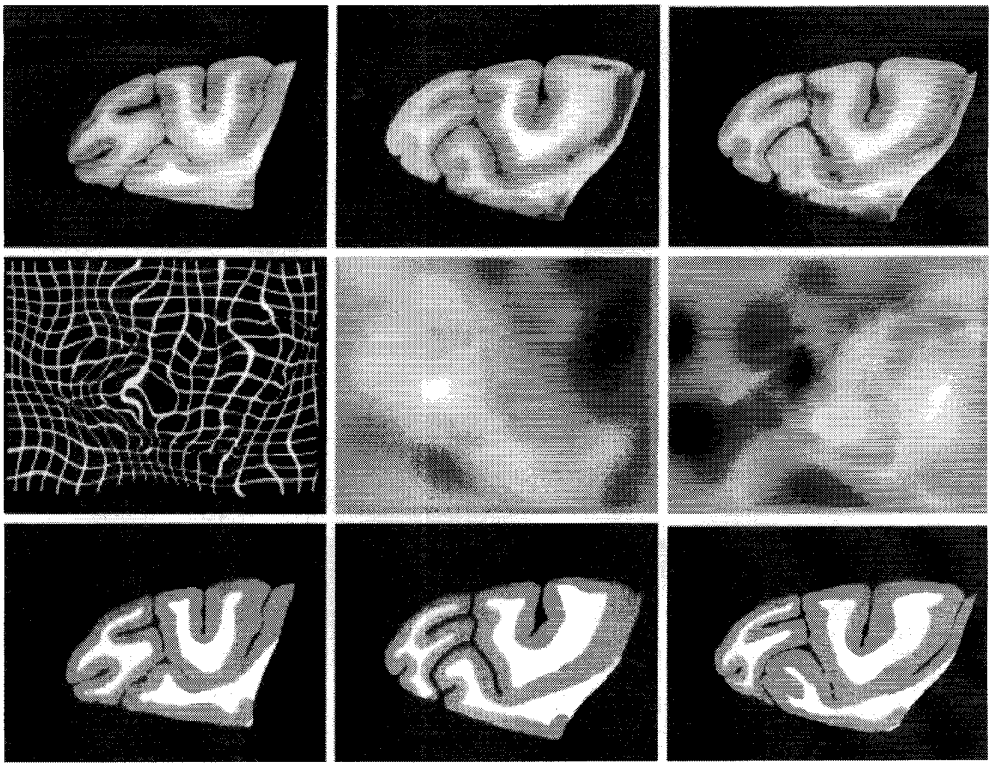

Fig. 5. Top-left panel shows the monkey visual cortex cryosection template and the top-middle panel shows the second monkey slice. The top-right panel shows the result of fluidly deforming the top-left into the top-middle anatomy. The middle row, left panel, shows the fluid transformation applied to the rectangular grid. The x- and y-components of the estimated transformation are shown in the middle row, middle and right panels, respectively. The bottom row shows a gray/white matter hand segmentation of the template (left) and study (middle). Shown in the bottom-right panel is an automatic segmentation of the study that was generated by applying the fluid transformation to the template segmentation.

where λ_o and μ_o are Lamé elastic material constants and I is the identity tensor. For small deformations the linear strain becomes $E = \frac{1}{2}[\vec{\nabla}\vec{u} + (\vec{\nabla}\vec{u})^T]$. Substituting this into Hooke's law and the momentum equation (2) gives

$$\mu_o \nabla^2 \vec{u} + (\lambda_o + \mu_o)\vec{\nabla}(\vec{\nabla} \cdot \vec{u}) + \vec{b}(\vec{u}) = 0 \qquad (11)$$

where we have neglected the inertial term, $\rho(d\vec{v}/dt) + \vec{v}\eta$.

It is straightforward to directly connect the PDE to the Bayesian posterior. For example, the momentum (3) and (17) arise via minimization of a Lagrangian according to

$$\hat{\vec{u}} = \arg\min_{\vec{u}} \int_t \left[\int_\Omega L^*(\vec{u}, \vec{x}, t)\, d\vec{x} + \alpha \int_\Omega C[T(\vec{x} - \vec{u}), S(\vec{x})]\, d\vec{x} \right] dt \qquad (12)$$

where L^* is the *generalized Lagrangian* energy density associated with constraints imposed by the linearized mechanics. For conservative systems, such as linear elasticity, L^* equals the total kinetic energy minus the potential energy [29], [34], and for nonconservative systems, such as viscous fluids, L^* is more complex [30]. Choosing

$$L^* = -\sum_{i=1}^{3}\sum_{j=1}^{3} \frac{\lambda_o}{2}\left[\frac{\partial u_i(\vec{x})}{\partial x_i}\right]\left[\frac{\partial u_j(\vec{x})}{\partial x_j}\right] + \frac{\mu_o}{4}\left[\frac{\partial u_i(\vec{x})}{\partial x_j} + \frac{\partial u_j(\vec{x})}{\partial x_i}\right]^2 \qquad (13)$$

substituting this energy density into (12), and setting the first variation equal to zero reproduces the momentum (11) for linear elasticity. Consider, for example the case of 3-D linear-elastic solid [27] where C is the energy of the Gibbs potential associated with the Gaussian cost between the study and the deformed template. Computing the first variation of the functional (12) shows that the forcing term $\vec{b}$ in the PDE [cf., (2), (3), (11)] is none other than the variation of the likelihood with respect to the transformation (5).

Since the PDE associated with linear elasticity has stress that depends only on the instantaneous strain independent of the path or history of the deformation, a *conservative* system results that can be represented as a variational problem that involves no real time. The path dependent stress-strain relationships such as required for the large-deformation viscous-fluid model presented here requires a formulation in space $\times$ time.

B. Viscous Fluid Versus Linear Elasticity

In previous work [6], linear-elasticity regularization was effectively used to enforce smoothness of the spatially sampled transformation. However, linear-elasticity penalizes large distance deformations thereby preventing the textbook from completely deforming into the study. As Fig. 2 demonstrates, the viscous fluid regularization does not have this property. This shortcoming in the elastic map is due to the quadratic

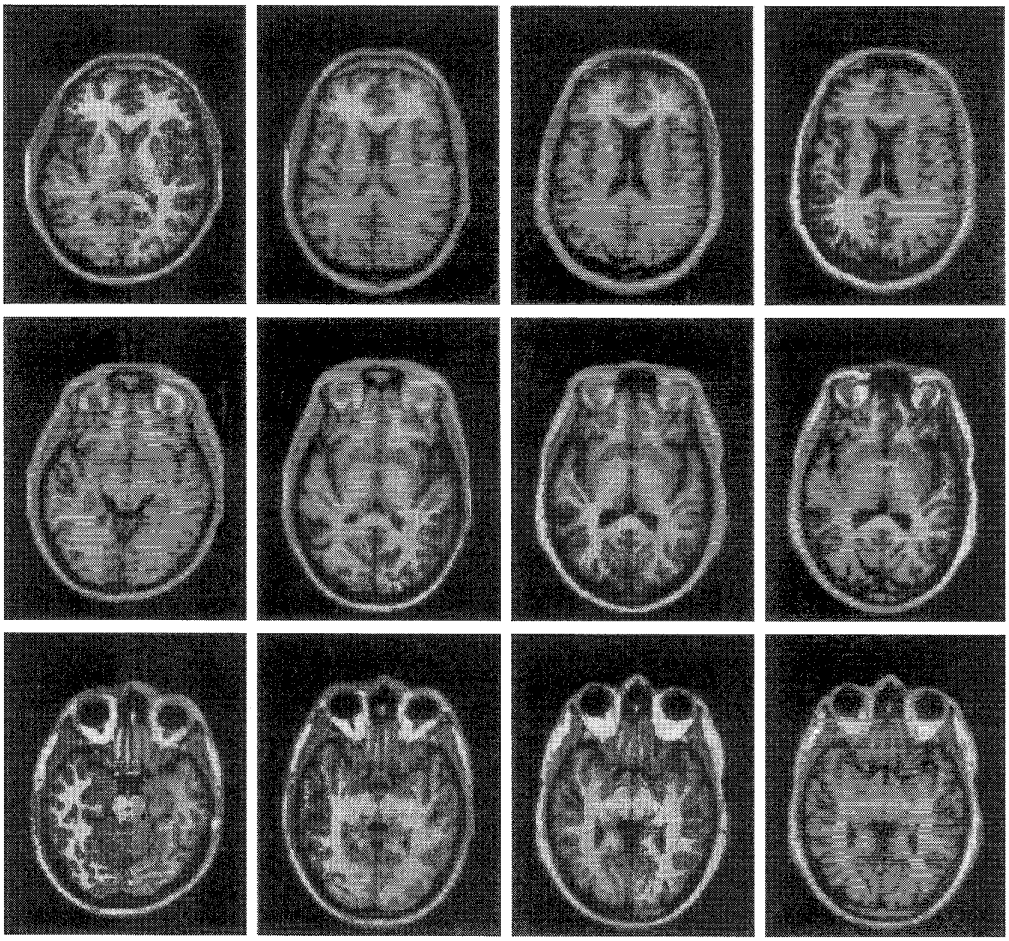

Fig. 6. 3-D deformation of a 128 × 128 × 100 MRI data set at 2 mm resolution. The rows (top to bottom) correspond to transverse slices 48, 55, and 60, respectively. The left column shows the undeformed template, the left-center column shows the 3-D elastic basis transformed template, the right-center column shows the 3-D fluid transformation that refined the elastic basis transformation, and the right column shows the target data set. Notice that the elastic basis transformation accommodated the global shape variation while the fluid transformation accommodated the local variation.

growth of the elasticity penalty and the inability of the linear elastic theory to address large magnitude deformations. The viscous-fluid regularization suffers from no such difficulties because the restoring forces relax over time, while at the same time accounting for the large distance kinematic nonlinearities.

The advantage of the fluid model for deforming one anatomy into another is demonstrated in Fig. 7. The rows from top to bottom correspond to a fluid, a strong elastic, and a weak elastic transformation of the monkey visual cortex. The left column shows the deformed template, the middle column shows the difference image between the deformed template and the study, and the right column shows the points in white where the Jacobian of the transformation is singular. Notice that the fluid model (top row) allowed the template to deform into the study as shown by the near-black difference image while maintaining a positive Jacobian. Conversely, the difference image for the transformation with the large elastic penalty (middle row) shows that the template was prevented from fully deforming into the study. The all-black Jacobian image for this transformation confirms that the large elastic transformation also has a positive Jacobian. The difference image for the weak elastic penalty (bottom row) shows that while the template was not held back as much as in the strong elastic case, it was still held back more than in the fluid case. In addition, the white points in its Jacobian image show that the transformation went singular and does not reflect a one-to-one mapping of volumes, areas, or lines [39].

The linear elasticity prior was derived assuming small angles of rotation and small linear deformations. Because it is assumed that the angles of rotation are small and the deformations are small and linear, large deformations cannot be accommodated with the linear PDE. This shortcoming of the linear elastic theory could be removed by using a hyperelastic energy form [35]. Accounting for the nonlinear kinematics would enforce a diffeomorphism, but would continue to penalize large magnitude deformations due to the elastic strain energy.

C. Parallel Computer Implementation

The elastic-solid basis and the fluid transformation algorithms were implemented on the massively parallel DECmpp 12 000Sx/Model 200 (MasPar). This computer is a 128×64

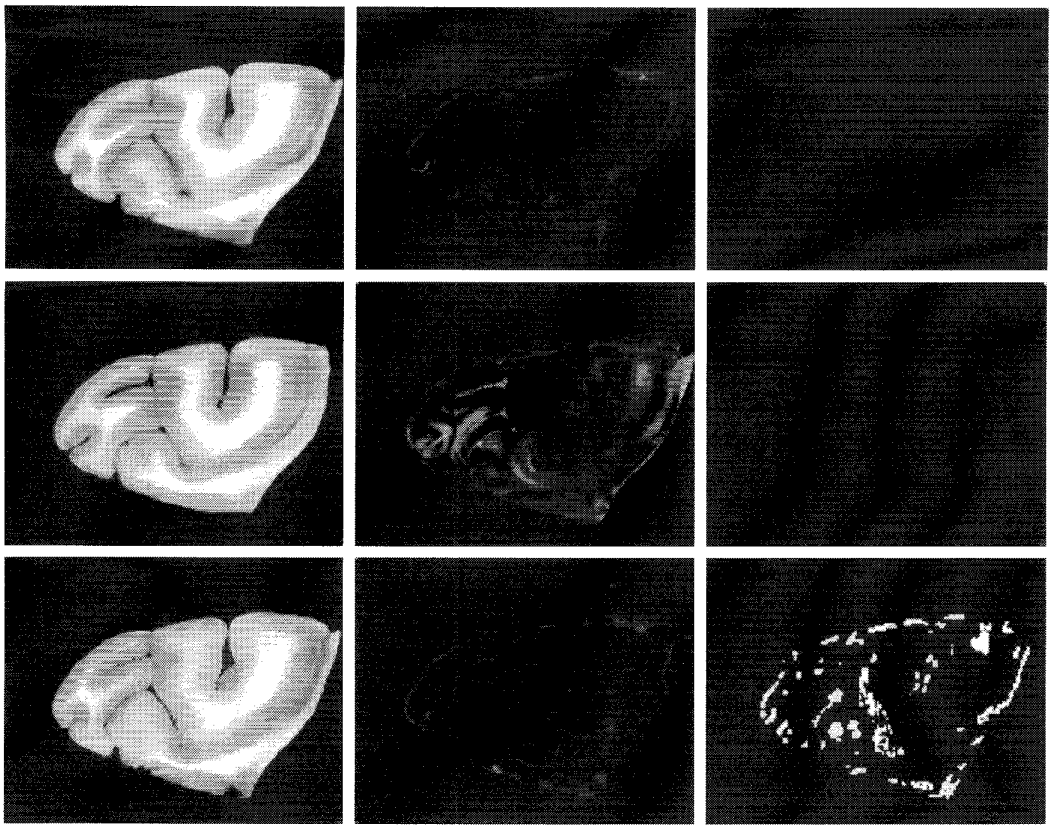

Fig. 7. The left column shows a fluid (top), a strong elastic (middle), and a weak elastic (bottom) transformation. The middle column shows the difference images between the deformed template and the study. The right column shows the negative Jacobian points of the deformation (right), respectively (cf. Fig. 5).

TABLE I
ELASTIC BASIS PROGRAM EXECUTION TIMES ON DECMPP 12 000SX

Experiment	data size	# of param. estimated	# of itrs	# of itrs before increasing basis	total time
2D monkey	128 × 128	242	200	20	33 sec
3D human	64 × 64 × 50	192	100	40	7.9 min

TABLE II
FLUID PROGRAM EXECUTION TIMES ON DECMPP 12 000SX

Experiment	data size	# of param estimated	# of iters	# PDE itrs	# of regrids	total time
patch to C	128 × 128	6.6×10^4	600	250	33	7.1 min
2D monkey	320 × 256	3.3×10^5	200	250	12	12.6 min
3D human	128 × 128 × 100	9.8×10^6	500	200	118	9.4 hours

mesh-connected single-instruction-multiple-data (SIMD) architecture, and is well suited for solving the elastic and fluid partial differential equations. Tables I and II show the timing results for the previous experiments. The second column of Table II shows the image sizes of the template and study images for each experiment. The number of parameters that were estimated for each experiment is shown in the third column. The number of relaxation iterations required to numerically satisfy (11) at each time step is shown in column five. These same algorithms would take over 10× longer to compute on a Silicon Graphics Power Challenge with one R8000 processor than on the 128 × 64 MasPar [40].

VI. SUMMARY

In this paper, we have presented a general approach for accommodating local shape variations by transforming the coordinate system of a template image into that of a target image. Specific computations were carried out for neuroanatomies of individual subjects with corresponding data appearing in an anatomical atlas. Global and local registration of the template and target images was achieved by first globally registering the template to the target image and then refining the transformation with the approach described in this paper. Results presented here are the first to accommodate the kinematic nonlinearities that are indeed necessary in order to maintain continuity of anatomical structures during the large-magnitude, local deformations. Formulation of the optimization problem is over a space-time continuum that takes into account not only the initial and final configurations of the template but also the path of the deformation. This allows relaxation of stress with time such that large magnitude deformations do not necessarily induce large penalties. Rather, large penalties result from rapid distortions of the underlying continuum and an infinite penalty results for any discontinuous deformations (i.e.,

$\vec{u}$ fields that cross and break up any region of the template). We have studied the constrained registration problem via solutions of associated PDE's. For the results presented here, the PDE's have been solved through direct numerical means on a massively parallel SIMD machine. We also note that due to the complexity of transformations that accommodate large-magnitude, nonlinear kinematics, further analysis and characterization of this new algorithm is required. We are currently working on ways to do this.

APPENDIX
FUNDAMENTAL CONSERVATION LAWS OF MECHANICS

In the field of continuum mechanics it is generally assumed that a control volume can be selected such that mass within the volume is conserved. For deformation of image templates, however, it is often desirable to allow the addition of mass (growth) or the subtraction of mass (shrinkage) on a local level. In order to allow for this we have reformulated the basic laws to account for a mass "creation" term. Derivation of the basic laws follows the classic method (reviewed by [37]) modified to include a spatially dependent mass source.

A. Conservation of Mass with a Mass Source

Consider a fixed volume Ω bounded by surface $\partial\Omega$. A source of mass supplies or extracts mass from the volume at a rate of η per unit volume. By conservation of mass the rate of mass change within the volume is equal to the rate of mass source minus the flux of mass through the surface. Using the divergence theorem, we obtain

$$\frac{d\rho}{dt} + \rho\vec{\nabla}\cdot\vec{v} = \eta \tag{14}$$

where d/dt is the material derivative, and the above equation is simply the differential form of the continuity equation with a mass source term.

B. Reynolds Transport Theorem with a Mass Source

In determining the equations describing conservation of momentum, it is necessary to determine the rate of change of a field variable associated with the material. The rate of change of the product $\psi\rho$ associated with the material instantaneously in a fixed volume Ω is equal to the rate of increase of $\psi\rho$ inside Ω plus the rate outward flux of $\psi\rho$ carried by mass transport through the volume surface $\partial\Omega$. Using the divergence theorem and applying the continuity equation with a mass source term (14) we find

$$\frac{d}{dt}\iiint_{\Omega}\rho\psi\,dV = \iiint_{\Omega}\left\{\rho\left[\frac{\partial\psi}{\partial t} + (\vec{\nabla}\psi)\cdot\vec{v}\right] + \psi\eta\right\}dV. \tag{15}$$

Equation (15) is a generalized version of the Reynolds transport theorem including a mass source term η.

C. Conservation of Momentum

Consider a fixed control volume Ω with boundary $\partial\Omega$. Traction stress $\vec{\tau}$ acts on the surface and a distributed body force $\vec{b}$ per unit volume acts on all material elements within the body. Applying Newton's Second Law in the form of conservation of linear momentum yields

$$\frac{d}{dt}\iiint_{\Omega}\rho\vec{v}\,dV = \iint_{\partial\Omega}\vec{\tau}\,dA + \iiint_{\Omega}\vec{b}\,dV \tag{16}$$

The traction force $\vec{\tau}$ is related to the stress tensor $\mathbb{T}$ by $\vec{\tau} = \mathbb{T}\cdot\vec{n}$ where $\vec{n}$ is the outward unit normal from the surface. Using this, the divergence theorem, and the generalized Reynolds transport theorem gives the equation for conservation of momentum with a mass source

$$\rho\frac{d\vec{v}}{dt} + \vec{v}\eta - \vec{\nabla}\cdot\mathbb{T} - \vec{b} = \vec{0}. \tag{17}$$

ACKNOWLEDGMENT

The authors are grateful to the following: S. Nadel, M.D., formerly of Duke University, for providing the 2-D MRI data; D. C. Van Essen, M.D., Ph.D., of the Department of Anatomy and Neurobiology at Washington University, for providing the cryosection data; and M. W. Vannier, M.D., of the Department of Radiology at Washington University, for providing the 3-D MRI data.

REFERENCES

[1] U. Grenander, Y. Chow, and D. Keenan, *HANDS: A Pattern Theoretic Study of Biological Shapes.* New York: Springer-Verlag, 1990.
[2] Y. Amit, U. Grenander, and M. Piccioni, "Structural image restoration through deformable templates," *J. Amer. Stat. Assoc.*, vol. 86, no. 414, pp. 376–387, June 1991.
[3] A. Knoerr, "Global models of natural boundaries," Pattern Anal. Rep. no. 148, Div. Appl. Math., Brown. Univ., 1988.
[4] U. Grenander and M. I. Miller. (1991) *Jump-diffusion processes for abduction and recognition of biological shapes.* Available: Electron. Signals Syst. Research Lab., Dept. of Elect. Eng., Washington Univ., St. Louis, MO.
[5] A. Srivastava, M. I. Miller, and U. Grenander, "Jump-diffusion processes for object tracking and direction finding," in *Proc. 29th Annual Allerton Conf. Comm., Contr. Comput.*, Univ. Illinois, Urbana-Champaign, IL, 1991, pp. 563–570.
[6] M. I. Miller, G. E. Christensen, Y. Amit, and U. Grenander, "Mathematical textbook of deformable neuroanatomies," *Proc. Nat Acad. Sci.* vol. 90, no. 24, Dec. 1993.
[7] G. E. Christensen, R. D. Rabbitt, and M. I. Miller, "A deformable neuroanatomy textbook based on viscous fluid mechanics," in *Proc. 27th Annual Conf. Inform. Sci. Syst.*, J. Prince and T. Runolfsson, Eds., Department of Electrical Engineering, The Johns Hopkins University, Baltimore, MD, Mar. 24–26, 1993, pp. 211–216.
[8] ——, "3-D brain mapping using a deformable neuroanatomy," *Physics Med. Biol.*, vol. 39, pp. 609–618, 1994.
[9] S. Joshi *et al.*,"Global shape models for optical sectioning microscopy," *J. Optic. Soc.*, Oct. 1992.
[10] M. I. Miller *et al.*,"Mitochondria, membranes and amoebae: 1, 2, and 3 dimensional shape models," in *Statistics and Imaging*, vol. II, K. Mardia, Ed. Abingdon: Carfax, 1994.
[11] U. Grenander, M. I. Miller, and G. E. Christensen, "Deformable anatomical data bases using global shape models: a position paper for the 1992 electronic imaging of the human body workshop," in *Proc. Coop. Working Grp. Whole Body 3-D Electron. Imaging Human Body*, Crew System Ergonomics Information Analysis Center, Wright Patterson Air Force Base, OH, Mar. 9–11, 1992.
[12] R. C. Buck, *Advanced Calculus*, 3rd ed. New York: McGraw-Hill, 1978.
[13] P. E. Undrill *et al.*,"Integrated presentation of 3d data derived from multi-sensor imagery and anatomical atlases using a parallel processing system," in *Proc. SPIE*, San Diego, CA, 1992, vol. 1653.
[14] C. A. Pelizzari *et al.*,"Accurate three-dimensional registration of CT, PET, and/or MR images of the brain," *J. Comput. Assisted Tomog.*, vol. 13, no. 1, pp. 20–26, 1989.

[15] P. T. Fox, J. S. Perlmutter, and M. E. Raichle, "A stereotactic method of anatomical localization for positron emission tomography," *J. Comput. Assisted Tomog.*, vol. 9, no. 1, pp. 141–153, 1985.
[16] U. Grenander and M. I. Miller, "Representations of knowledge in complex systems," *J. Royal Stat. Soc. B*, vol. 56, no. 3, 1994.
[17] A. Hill, T. F. Cootes, C. J. Taylor, and K. Lindley, "Medical image interpretation: A generic approach using deformable templates," *Med. Informat.*, vol. 19, no. 1, pp. 47–59, 1994.
[18] T. F. Cootes, C. J. Taylor, D. H. Cooper, and J. Graham, "Active shape models—their training and application," *Comput. Vision Image Understand.*, vol. 61, no. 1, pp. 38–59, 1995.
[19] D. Metaxas and D. Terzopoulos, "Shape and nonrigid motion estimation through physics-based synthesis," *IEEE Trans. Pattern Anal. Machine Intell.*, vol. 15, no. 6, pp. 580–591, 1993.
[20] R. Szeliski, *Bayesian Modeling of Uncertainy in Low-Level Vision.* Boston: Kluwer, 1989.
[21] D. Terzopoulos and K. Waters, "Physically based facial modeling, analysis, and animation," *J. Visual. Comput. Animation,* vol. 1, pp. 73–80, 1990.
[22] R. Bajcsy, R. Lieberson, and M. Reivich, "A computerized system for the elastic matching of deformed radiographic images to idealized atlas images," *J. Comput. Assisted Tomog.*, vol. 7, no. 4, pp. 618–625, 1983.
[23] R. Bajcsy and S. Kovacic, "Multiresolution elastic matching," *Comput., Vision, Graphics, Image Processing,* vol. 46, pp. 1–21, 1989.
[24] G. Wahba, *Spline Models for Observational Data.* Philadelphia, PA: Soc. Industrial Applied Math., 1990.
[25] F. L. Bookstein, *Morphometric Tools for Landmark Data.* Cambridge, UK: Cambridge Univ. Press, 1991.
[26] S. Timoshenko, *Theory of Elasticity.* New York: McGraw-Hill, 1934.
[27] L. A. Segel, *Mathematics Applied to Continuum Mechanics.* New York: Dover, 1987.
[28] L. Meirovitch, *Analytical Methods in Vibrations.* New York: McMillan, 1967.
[29] J. N. Reddy, *Energy and Variational Methods in Applied Mechanics.* New York: Wiley-Interscience, 1984.
[30] L. Mittag, M. J. Stephen, and W. Yourgrau, "Variational principles in hydrodynamics," in *Variational Principles in Dynamics and Quantum Theory,* W. Yourgrau and S. Mandlestam, Eds. New York: Dover, 1979.
[31] E. R. McVeigh, R. M. Henkelman, and M. J. Bronskill, "Noise and filtration in magnetic resonance imaging," *Med. Physics,* vol. 12, no. 5, pp. 586–591, 1985.
[32] D. L. Snyder, Jr., L. J. Thomas, and M. M. Ter-Pogossian, "A mathematical model for positron emission tomography systems having time-of-flight measurements," *IEEE Trans. Nuclear Science,* vol. NS-28, pp. 3575–3583, 1981.
[33] D. L. Snyder, A. M. Hammoud, and R. L. White, "Image recovery from data acquired with a charge-coupled-device camera," *J. Optic. Soc. Amer. A,* vol. 10, pp. 1014–1023, 1993.
[34] B. D. Vujanovic and S. E. Jones, "Variational methods in nonconservative phenomena," in *Mathematics Science Engineering,* vol. 182. New York: Academic, 1989.
[35] J. C. Simo, "A framework for finite strain elastoplasticity based on maximum dissipation and the multiplicative decomposition: part I, continuum formulation," *Computat. Methods Appl. Mechanics Eng.*, vol. 66, pp. 199–219, 1988.
[36] B. Horn, *Robot Vision.* Cambridge, MA: MIT Press, 1986.
[37] L. E. Malvern, *Introduction to the Mechanics of a Continuous Medium.* Englewood Cliffs, NJ: Prentice-Hall, 1969.
[38] J. C. Strikwerda, *Finite Difference Schemes and Partial Differential Equations.* Pacific Grove, CA: Wadsworth and Brooks/Cole, 1989.
[39] G. E. Christensen *et al.*: "Topological properties of smooth anatomic maps," in *Information Processing in Medical Imaging,* vol. 3, Y. Bizais, C. Braillot, and R. DiPaola, Eds. Norwell, MA: Kluwer, June 1995, pp. 101–112.
[40] G. E. Christensen, M. I. Miller, U. Grenander, and M. W. Vannier, "Individualizing Neuroanatomical Atlases Using a Massively Parallel Computer," *IEEE Computer*, pp. 32–38, Jan. 1996.

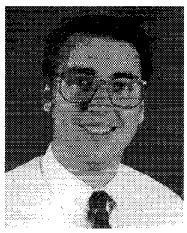

Gary E. Christensen (S'86–M'95) received the B.S. degrees in electrical engineering and computer science, (magna cum laude) from Washington University, St. Louis, MO, in 1988, and the M.S. and D.Sc. degrees in electrical engineering from Washington University in 1989 and 1994, respectively.

In 1994, he joined the faculty of the Washington University School of Medicine, where he is currently an Assistant Professor in the Mallinckrodt Institute of Radiology and the Department of Surgery. He is also the Director of the Craniofacial Imaging Laboratory, St. Louis Children's Hospital, Washington University Medical Center. His primary research interests include image processing, 3-D visualization, medical imaging, computer architecture, parallel computing, and deformable shape models.

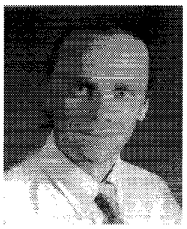

Richard D. Rabbitt earned the B.S. and M.S. degrees in mechanical engineering from Michigan State University, East Lansing, MI, in 1980 and 1982, respectively. In 1986, he was awarded the Ph.D. in mechanics from Rensselaer Polytechnic Institute, Troy, NY, where he also studied as a postdoctoral research associate in applied mathematics.

From 1987 to 1994, he was an Assistant Professor of mechanical engineering at Washington University, St. Louis, MO. He was selected a Presidential Young Investigator by the National Science Foundation in 1988 for his work on the biomechanics of hearing. He is currently an Associate Professor of bioengineering at the University of Utah, Salt Lake City, with primary specialization in the biomechanics of soft tissues.

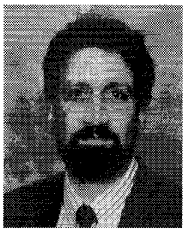

Michael I. Miller (SM'95) received the B.S. degree in electrical engineering from the State University of New York, Stony Brook, in 1976. He received the M.S. degree in electrical engineering in 1978 and the Ph.D. in biomedical engineering in 1983, both from Johns Hopkins University, Baltimore, MD.

In 1983, he joined the Electrical Engineering Department, Washington University, St. Louis, MO, where he is a Professor of Electrical Engineering. He is also a full professor at the Mallinckrodt Institute of Radiology at Washington University, and at the Institute for Biomedical Computing. His current research interests include automated target recognition, medical imaging, computational linguistics, pattern theory, stochastic processes, and computational neuroscience. Dr. Miller is the Director of the Army Center for Imaging Science, a consortium of universities involving Washington University, Harvard University, Massachusetts Institute of Technology, and the University of Texas.

He is a recipient of a Presidential Young Investigator Award, and currently holds the Newton R. and Sarah L. Wilson Professorship in Biomedical Engineering.